

# CHANDRA ANALYSIS AND MASS ESTIMATION OF THE LENSING CLUSTER OF GALAXIES CL0024+17

NAOMI OTA<sup>1,2,3</sup>, ETIENNE PONTECOUTEAU<sup>4</sup>, MAKOTO HATTORI<sup>5</sup>, AND KAZUHISA MITSUDA<sup>3</sup>  
*Draft Version October 8, 2003*

## ABSTRACT

We present a detailed analysis of *Chandra* X-ray observations of the lensing cluster of galaxies CL0024+17 at  $z = 0.395$ . We found that the radial temperature profile is consistent with being isothermal out to  $\sim 600$  kpc and that the average X-ray temperature is  $4.47^{+0.83}_{-0.54}$  keV. The X-ray surface brightness profile is represented by the sum of extended emission centered at the central bright elliptical galaxy with a small core of 50 kpc and more extended emission which can be well described by a spherical  $\beta$ -model with a core radius of about 210 kpc. Assuming the X-ray emitting gas to be in hydrostatic equilibrium, we estimated the X-ray mass within the arc radius and found it is significantly smaller than the strong lensing mass by a factor of about 2–3. We detected a strong redshifted iron K line in the X-ray spectrum from the cluster for the first time and find the metal abundance to be  $0.76^{+0.37}_{-0.31}$  solar.

*Subject headings:* galaxies: clusters: individual (CL0024+17) — X-rays: galaxies — gravitational lensing — dark matter

## 1. INTRODUCTION

CL0024+17 is one of the most extensively studied distant clusters of galaxies, located at  $z = 0.395$ . The cluster is known to exhibit spectacular multiple arc images of a background galaxy produced by the gravitational lens effect. This makes the cluster a unique target for studying the distribution of not only luminous matter but also dark matter.

The lensed arc system was initially noted by Koo (1988) and the first spectroscopic observation placed limits on the arc redshift,  $1 < z_{\text{arc}} < 2$  (Mellier et al. 1991). From the deep HST imaging, four arc images of the blue source galaxy were identified around the tangential critical curve and further was a radial arc of the same source (Smail et al. 1996; Colley et al. 1996). In addition, CL0024+17 is the first cluster where a coherent weak shear signal was detected (Bonnet et al. 1994).

The remarkably well-resolved lens images allow detailed modeling of the dark matter distribution in the cluster center and several authors have attempted the mass reconstruction (Kassiola et al. 1992; Smail et al. 1997; Tyson et al. 1998; Broadhurst et al. 2000). Tyson et al. (1998) has built a very detailed mass map comprising 512 free parameters. They found that, excluding the mass associated with individual galaxies, the dark mass distribution is smooth and has little asymmetry, and the central profile has a soft core of  $35 h^{-1}$  kpc. This is contradictory to the central cusp predicted by the CDM numerical simulations (Navarro et al. 1996, hereafter NFW) and thus has motivated investigations of different types of dark matter such as self-interacting dark matter (Spergel & Steinhardt 2000; Moore et al. 2000). Broadhurst et al. (2000) measured the arc redshift to be  $z_{\text{arc}} = 1.675$  and also built a lens model in a simplified manner assuming NFW pro-

files for cluster galaxies. Their model needed to include only the brightest eight cluster galaxies to reproduce the observed lensed configuration. They reached the conclusion that, in contrast to Tyson et al. (1998)'s model, the average mass profile is consistent with an NFW profile. Shapiro & Iliev (2000) pointed out that the fit by Broadhurst et al. (2000) implies a cluster velocity dispersion that is much larger than the value measured for this cluster by Dressler et al. (1999).

The galaxy velocity dispersion of  $\sigma \simeq 1200$  km/s was found by Dressler & Gunn (1992) and Dressler et al. (1999) based on the data of about 100 galaxies. Czoske et al. (2001, 2002) constructed a galaxy catalog of the wide-field spectroscopic survey of the cluster, and newly identified a foreground and a background group of galaxies well aligned along the line of sight. They clearly demonstrated the bimodal distribution of galaxies in the redshift histogram for 300 objects in the neighborhood of CL0024+17. If restricted to the galaxies in the main component, the velocity dispersion is  $\sim 600$  km/s. Thus if interpreted as a value for a relaxed cluster, the dynamical mass would have only a quarter of that previously derived (Schneider et al. 1986).

X-ray emitting intracluster gas is an excellent tracer of the dark matter potential. Soucail et al. (2000) performed a combined analysis of the *ROSAT* and the *ASCA* data and estimated the cluster mass within the arc radius under the assumption of hydrostatic equilibrium (the X-ray mass, hereafter). They found that there is about a factor of  $\sim 3$  discrepancy between the X-ray mass and the strong lensing mass (Tyson et al. 1998; Broadhurst et al. 2000). They compared the extrapolated X-ray mass to the weak lensing mass within  $3 h_{50}^{-1}$  Mpc and found it is again lower by a factor of  $\sim 3$ . Because the *ROSAT* HRI image suggested an elongated gas distribution (see also Böhringer

<sup>1</sup> Department of Physics, Tokyo Metropolitan University, 1-1 Minami-osawa, Hachioji, Tokyo 192-0397, Japan

<sup>2</sup> naomi@phys.metro-u.ac.jp

<sup>3</sup> Institute of Space and Astronautical Science, Sagamihara, Kanagawa 229-8510, Japan

<sup>4</sup> CEA/Saclay, L'Orme des Merisiers, 91191 Gif sur Yvette, France

<sup>5</sup> Tohoku University, Aoba Aramaki, Sendai 980-8578, Japan

et al. 2000), they considered that the discrepancy may be partly caused by the irregular mass distribution.

The ‘mass discrepancy problem’ between X-ray and strong lensing mass estimation has been reported in many other lensing clusters and the X-ray mass is systematically lower than the strong lensing mass by a factor of 2–5 (Miralda-Escude & Babul 1995; Wu & Fang 1997; Ota et al. 1998; Hashimoto-dani 1999). A variety of possible explanations have been proposed; non-thermal pressure support, effect of complex mass distribution, etc. (e.g. Hattori et al. 1999). However, there is as yet no definitive explanation, and it is possible that some important physical process may not have been considered in regard to the central region of clusters.

For the specific case of CL0024+17, however, there were still large measurement uncertainties in both the X-ray temperature and the image morphology, due mainly to heavy contamination from a bright seyfert galaxy that lies near the cluster center. Thus for the cluster mass estimation the temperature determination is crucial. The high-resolution *Chandra* data eliminate the contamination from point sources and enable us to determine the X-ray spectrum and the spatial distribution of the cluster gas simultaneously. In this paper, we report accurate measurements of the temperature and the morphology with *Chandra*, from which we consider the discrepancy between the X-ray and the strong lensing masses.

We use  $H_0 = 50 \text{ km/s/Mpc}$  and  $\Omega_0 = 1$ , and thus  $1'$  corresponds to  $383 h_{50}^{-1} \text{ kpc}$  at  $z = 0.395$ . The quoted errors are the 90% confidence range throughout the paper, except where noted. We use the solar abundance ratio of iron atoms to hydrogen atoms,  $\text{Fe/H} = 4.68 \times 10^{-5}$  (Anders & Grevesse 1989).

## 2. OBSERVATION AND SOURCE DETECTION

### 2.1. *Chandra* observation of CL0024+17

We observed CL0024+17 with the *Chandra* Advanced CCD Imaging Spectrometer (ACIS-S) detector on September 20, 2000. The target was offset from the ACIS-S nominal aimpoint with a Y offset of  $-1'.33$  in order to avoid the outskirts of cluster diffuse emission falling in a gap between the CCD chips. The CCD temperature was  $-120^\circ\text{C}$ . The data were reduced using CIAO version 2.2 with CALDB version 2.15. We removed periods of high background levels exceeding  $3\sigma$  above the mean quiescent background rates. The net exposure time was 37121 sec (93.2% of the total exposure). To improve the *Chandra* astrometry we used the Aspect Calculator and corrected the aspect offsets. In Figure 1, we show the ACIS-S3 image in the 0.5–7 keV band. The strongest X-ray peak of CL0024+17 is at  $00:26:36.0, +17:09:45.9$  (J2000) and extended emission is detected out to  $\sim 2'$  in radius. We refer to the X-ray peak as the G1 peak hereafter.

We planned to set the roll angle at  $127^\circ$  with a tolerance of  $\pm 8^\circ$  in order to place the position of the “perturbation”, indicated by the weak lensing analysis (Bonnet et al. 1994), on the ACIS-I2 chip. The perturbation is about  $6'.7$  north-northeast of the gravitational shear coherent to the CL0024+17 center. However the tolerance was exceeded by  $8'.4$  and the actual roll angle was  $135.14^\circ$ , and thus the perturbation was outside the ACIS field of view.

### 2.2. Source detection in the ACIS-S3

We searched for point-like sources in the ACIS-S3 field with the WAVDETECT algorithm with a significance threshold parameter of  $10^{-6}$  and detected 38 sources. In the following analysis these point sources were excluded with a radius of 7 times the size of the point spread function (PSF) at the source position. The PSF size is defined as the 40% encircled energy radius at 1.5 keV. We cross-correlated the source positions with the *ROSAT* HRI and found 5 sources in the ACIS-S3 field of view (S1, S2, S3, S4, S5 in Soucail et al. 2000) were consistent with each other within  $1'' \sim 3''$ , which is smaller than the pointing accuracy of the *ROSAT* HRI ( $1\sigma$  error is typically  $6''$ ; Briel et al. (1997)). For S1, there were two optical counterparts within the *ROSAT* error box ( $16'' \times 16''$ ), which are a foreground starforming galaxy and one of the cluster member galaxies. The *Chandra* imaging clearly resolved S1 into two point sources, whose J2000 coordinates are respectively determined to be  $(\alpha, \delta) = (00:26:31.691, +17:10:21.71)$  and  $(00:26:31.101, +17:10:16.48)$ . These are cataloged by Czoske et al. (2001) as #282 ( $z = 0.2132$ ) and #267 ( $z = 0.4017$ ) respectively, thus by comparing the positions we confirmed that the *Chandra* astrometry is accurate down to  $0''.3$ .

### 2.3. MG0023+171

The radio source MG0023+171 with  $z = 0.946$  (Hewitt et al. 1987) was covered with the ACIS-S0 chip during the observation. MG0023+171 has two optical counterparts separated by  $5''$  which have been interpreted as gravitationally lensed images. The large separation angle implies a large mass-to-light ratio for the lensing matter however the lensing object has not yet been identified. We searched for X-ray emission from a “dark object”, but did not detect any object using WAVDETECT with the threshold parameter of  $10^{-5}$ . The photon counts in the 0.5–7 keV band within a circle of radius  $5''$  centered at image A of MG0023+171 system is 6, without subtracting background. We thus constrained the  $3\sigma$  upper limit on the X-ray energy flux as  $8.3 \times 10^{-15} \text{ erg/s/cm}^2$  assuming a power-law spectrum with the photon index of 2.0. On the other hand if we extrapolate the B magnitude of the radio source, 21.9, utilizing a typical  $\alpha_{\text{OX}}$  index for radio-loud quasars of 1.6 (Green et al. 1995), the X-ray flux at 2 keV is expected to be  $6.4 \times 10^{-16} \text{ erg/s/cm}^2/\text{keV}$ . We found that this is below the detection limit of the current observation. If we attribute the entire X-ray flux to a lensing object at an assumed redshift of 0.4, the upper limit of the X-ray luminosity is constrained to be  $\sim 7 \times 10^{42} \text{ erg/s}$ . Thus a massive object such as a galaxy group or a galaxy cluster is unlikely to be the dark lens candidate as long as one assumes the normal X-ray properties.

## 3. SPECTRAL ANALYSIS

### 3.1. Overall spectrum

We extracted the cluster spectrum from a circular region of  $r = 1'.5$ , centered on the G1 peak. The background was estimated from the  $2'.5 < r < 3'.2$  ring region and subtracted from the above spectrum. Note that we investigated the positional dependency of the background by

comparing two spectra accumulated in the corresponding detector regions for the source and the background spectra of the blank-sky observation data. We found that the difference of the background spectra from the two regions is sufficiently small (the difference in intensity is less than 20% in each spectral bin and the overall normalization deviates by 4%) and the results of the present analysis are not affected within the statistical errors. We generated the telescope response file (i.e. the ARF file) for an extended source with the WARF procedure, which sums the ARFs according to the weight of counts in each bin in the given image region. We found that the weighted ARF differs only by 2% at most in the ACIS-S energy band from that made for a point source. Thus effect of telescope vignetting is negligible in comparison to the statistical errors of the present data.

We fitted the cluster spectrum in the energy range of 0.5 – 7 keV with the MEKAL thin-thermal plasma model (Mewe et al. 1985, 1986; Kaastra 1992; Liedahl et al. 1995). If we include the hydrogen column density of the neutral absorption as a free parameter, we obtained  $N_{\text{H}} = (5.3 \pm 2.5) \times 10^{20} \text{ cm}^{-2}$ . This is consistent with the Galactic value, thus we fixed it at  $N_{\text{H}} = 4.2 \times 10^{20} \text{ cm}^{-2}$  (Dickey & Lockman 1990). The result of the fit is shown in Figure 2 and Table 1. This provided a good fit to the data and the resulting  $\chi^2$  value was 47.5 for 45 degrees of freedom. The temperature was determined to be  $kT = 4.47$  keV with the 90% error range of 3.93 – 5.30 keV. The result is consistent with the previous measurement with *ASCA*, which had a large ( $\sim 50\%$ ) uncertainty (Soucail et al. 2000).

We detected strong line emission at about 4.8 keV in our reference frame, which is consistent with a redshifted, highly ionized Fe-K line emitted from an object at  $z = 0.395$ . This is the first detection of the iron line from CL0024+17. We obtained the metal abundance to be  $0.76^{+0.37}_{-0.31}$  solar (90% error). In the *Chandra* spectrum there is also a significant contribution from the Fe-L complex below 1 keV. If we mask the energy bins between 4 keV and 5.2 keV that cover the energy of Fe-K line, the MEKAL model fitting resulted in the metal abundance of  $1.38^{+1.63}_{-0.65}$  solar (90% error). The best-fit value is higher than that we obtained from the above fit however still consistent within the error ranges. Thus the metallicity for CL0024+17 is about a factor of 2 higher than those of typical distant clusters (Mushotzky & Loewenstein 1997; Matsumoto et al. 2000; Ota 2001). On the other hand, the previous *ASCA* spectral analysis by Soucail et al. (2000) did not constrain iron emission lines because the photon statistics of the cluster spectrum were seriously limited due to the contamination from the S1 emission. The high metallicity value we derived is discussed later in the paper (See §6.1). The X-ray luminosity in the 0.5 – 7 keV is  $3.4 \times 10^{44} \text{ erg/s}$ . The bolometric luminosity is estimated to be  $5.1 \times 10^{44} \text{ erg/s}$ .

### 3.2. Radial temperature distribution

In order to investigate the radial temperature profile, we accumulated spectra from four annular regions centered on the G1 peak. The radius ranges were chosen so that each spectrum contains more than 400 photons. We fitted the spectra with the MEKAL model to determine the tem-

peratures, where the neutral absorption was fixed at the Galactic value and the metallicity of the gas was allowed to vary. In Figure 3(a), we plot the radial temperature profile and  $1\sigma$  error bars. The temperature in each radial bin was constrained with  $13 \sim 20\%$  accuracy. We found that there is no meaningful temperature variation with radius.

We further restrict the spectral regions to  $8''$  and  $4''$  ( $= 51$  and  $26 h_{50}^{-1} \text{kpc}$ ) from the G1 peak to constrain the X-ray emission from G1. From the MEKAL model fitting to the spectra, we obtained the X-ray temperature to be 3.7 (2.7–5.5) keV and 3.4 (2.6–4.6) keV for the regions of  $r < 4''$  and  $8''$ , respectively. Thus the temperature is still higher than 2.6 keV (90% confidence) at the center.

From the above analysis, we found that the intracluster gas is consistent with being isothermal out to  $\sim 600 h_{50}^{-1} \text{kpc}$ . Note that the fraction of the maximum radius to the virial radius,  $r_{200}$  (See §6.1 for definition) is 0.41. In Figure 3(b), we show the 68% confidence contours for the temperature and the metallicity for four annular regions obtained from the MEKAL model fitting. We found that the best-fit metallicity at the cluster center is as high as 1 solar, however, due to the large statistical errors the abundance gradient is not significant.

## 4. IMAGE ANALYSIS

### 4.1. X-ray surface brightness and galaxy distribution

Though the original ACIS CCD has a pixel size of  $0''.492$ , we rebinned the image increasing the bin dimensions by a factor of 4. Thus 1 image pixel is  $1''.968$  which is 12.6 kpc at the cluster's frame. We restrict the energy range to 0.5 – 5 keV in the image analysis in order to avoid the hard energy band where the background dominates the total spectrum. We find that there is a second X-ray peak at 00:26:35.1, +17:09:38.0 (J2000). We refer to the second X-ray peak as G2 hereafter. The G2 peak is about 100 kpc southwest of the G1 peak. We investigated the correlation between the X-ray surface brightness and the member galaxies cataloged by Czoske et al. (2001). As shown in Figure 5a, by superposing the galaxies with redshift range of 0.38 – 0.41 and V magnitude smaller than 22 on the *Chandra* X-ray image, we recognized that the three central bright elliptical galaxies are located at positions that coincide with the G1 and the G2 X-ray peaks. The object numbers and the redshifts cataloged by Czoske et al. (2002) are #380 ( $z = 0.3936$ ), #374 ( $z = 0.3871$ ), and #362 ( $z = 0.3968$ ) from east to west in Figure 5a. Note that G1 contains #380 and #374 however the X-ray peak position is more consistent with #380 (Figure 5a).

### 4.2. 1-D fitting of the X-ray surface brightness distribution

We investigate the X-ray surface brightness distribution by 1-dimensional and 2-dimensional model fitting in this and the next subsection, respectively. The latter is more precise in the sense that the central position of the X-ray emission can be included as a model parameter. Here we derive an azimuthally averaged surface brightness distribution centered at the strongest peak, G1, from the 0.5–5 keV image and evaluate the overall shape by fitting a  $\beta$ -model,  $S(r) = S_0(1 + (r/r_c)^2)^{-3\beta+1/2}$  (Cavaliere & Fusco-Femiano 1976). The telescope vignetting was corrected by dividing the image with the exposure map. The G2 peak

was excluded with a circular region of  $4''$  in radius, which covers more than 95% of the G2 emission, when calculating the profile.

We found that a single-component  $\beta$ -model is rejected at the 99.1% level and there is clearly strong excess emission over the model in the innermost region (Figure 4a). We also notice that there is a point of inflection in the profile at around  $r \sim 100$  kpc, where systematic variation of the residuals are clearly visible. This leads us to test the hypothesis that the surface brightness consists of two components. If we introduce a double- $\beta$  model consisting of two  $\beta$ -profiles with different core radii, the fit was significantly improved from the single  $\beta$  model and gave  $\chi^2/\text{dof} = 183.2/194$ . In Figure 4b, we show the results for the double  $\beta$ -model fitting. The derived parameters are listed in Table 2. Note that the background constant was included as a free parameter in the fit and determined to be  $C = 8.5^{+0.3}_{-0.2} \times 10^{-9}$  counts/sec/cm<sup>2</sup>. A strong degeneracy exists between parameters  $r_{c,in}$  and  $\beta_{in}$  (i.e. the core radius and the slope for the inner component of the double  $\beta$ -model) that prevents the fit from converging properly. We tried different fixed values of  $\beta_{in}$  ranging between 0.5 and 1.5 and found that all fitting parameters except for  $r_{c,in}$  are consistent with the result for  $\beta_{in} = 1$  within the 90% error bars. As long as  $0.6 \leq \beta_{in} \leq 1.5$  the resultant  $r_{c,in}$  value is also statistically consistent with the result for  $\beta_{in} = 1$ . Thus we chose to fix  $\beta_{in}$  to 1.

We also tested a model for gas distribution in the case that the gas is in hydrostatic equilibrium in the NFW potential (Navarro et al. 1996). Suto et al. (1998) provided a useful fitting formula for the X-ray surface brightness distribution in the generalized form of the NFW-type potential,  $\rho(x) \propto 1/(x^\alpha(1+x)^{3-\alpha})$ , which gives a good fit for  $1.0 \leq \alpha \leq 1.6$ . We refer to the formula (i.e. equation 29–32 in Suto et al. 1998) as the NFW-SSM model hereafter. It is also known that the gas density profile for the NFW model is well approximated by the  $\beta$ -model (Makino et al. 1998), though it has a slightly steeper slope in the innermost region. Thus it is worth quantifying the parameter  $\alpha$ . We first fitted the radial surface brightness distribution with the NFW-SSM model for  $\alpha = 1$  (i.e. the NFW case). The result is presented in Table 2. We found that it is not accepted at the 90% confidence level. If the  $\alpha$  value is allowed to vary within the range 1.0 to 1.6, we found that the  $\alpha = 1.6$  case resulted in the minimum  $\chi^2$  value of 199.8 for 196 degrees of freedom. Thus the central X-ray profile appears to be much steeper than that expected from the original NFW profile. However the model with  $\alpha = 1.6$  is unlikely because  $r_s$  became unrealistically large (more than one order of magnitude larger than the value for the  $\alpha = 1$  case).

Thus from the 1-dimensional analysis, the X-ray spatial distribution is not sufficiently described either by the single-component  $\beta$ -model or by the NFW-SSM model and is significantly better fitted with the double- $\beta$  model.

#### 4.3. 2-D fitting of the X-ray surface brightness distribution

In order to determine the X-ray emission profile of the ICM more precisely, we fitted the 2-dimensional surface brightness distribution with a model consisting of three  $\beta$  profiles which we consider to represent emission from

two compact components associated with the G1 and the G2 peaks and “cluster” component and the constant background;

$$S(r) = \sum_{i=1}^3 S_{0,i} (1 + (r/r_{c,i})^2)^{-3\beta_i + 1/2} + C. \quad (1)$$

We fitted the image of the central ( $100$  image pixel)<sup>2</sup> = ( $3'.3$ )<sup>2</sup> region using the maximum-likelihood method. The center positions of the first two compact components were fixed at the G1 and the G2 peaks, respectively, while for the third component, which we consider describes the ICM emission, the position was allowed to vary. Because the slope parameters for the G1 and the G2 components were insensitive to the fit, we first assumed King profiles (King 1962), namely  $\beta$  models with  $\beta_1 = \beta_2 = 1$ . The core radius of G2 was not resolved with the spatial resolution of the current image analysis, thus fixed at  $r_2 = 10$  kpc as is typical for an elliptical galaxy. The background level,  $C$ , was fixed at the value that was estimated from the 1-D analysis,  $8.5 \times 10^{-9}$  counts/sec/cm<sup>2</sup>. We performed the fit with the SHERPA package, where we included the exposure map to convolve the model image with the telescope and detector responses. The exposure map was calculated at an energy of 0.8 keV, representative of the spectral energy distribution. The results of the fits are shown in Table 3 and Figure 5. In order to check the goodness of the fit, we rebinned the image into two single dimensional profiles in the right ascension and declination directions (Figure 5d) and calculated the  $\chi^2$  values between the model and data profiles to find they are sufficiently small ( $\chi^2/\text{dof} = 112.4/99$  and  $108.2/99$  for the  $\alpha$ - and  $\delta$ -directions, respectively). The best-fit cluster center position is significantly shifted from the G1 peak by  $12''.5$ , that is  $80 h_{50}^{-1}$  kpc, towards the southwest direction. There is no optical counterpart present at this position.

In Table 3, the results of 2-dimensional image fitting are listed. For G1 we obtained a core radius of  $52^{+11}_{-9}$  kpc. The cluster component was found to be much more extended than the G1 component, being described by a spherical  $\beta$ -model with  $r_{c,3} = 210^{+33}_{-30}$  kpc and  $\beta_3 = 0.71^{+0.07}_{-0.06}$ . The 90% confidence contour of the  $\beta_3$  and  $r_{c,3}$  are shown in Figure 6. These two values are consistent with those we obtained from the 1-D fitting even though the cluster center is significantly displaced from that assumed in the 1-D analysis. We consider that this is because the displacement is small in comparison to the cluster core radius, inside which the surface brightness is flat. The small core radius of the G1 emission is consistent with the result from the ROSAT HRI though it gave a smaller  $\beta$  value. In fact we obtained a similarly small  $\beta$  in the 1-D analysis (see §4.2). This may be naturally explained by the existence of emission from the larger core component. In addition, though we fixed the  $\beta_1$  value at 1 for G1 because the inner slope parameter is not sensitive to the fit, as for the 1-D fitting, we confirmed that the resultant  $\beta$ -model parameters for all three components do not change within statistical errors if  $0.6 \leq \beta_1 \leq 1.5$ .

We estimated the luminosities for the three components by dividing the total luminosity obtained from the spectral fit according to the ratio of photon counts between the three. Here we assumed isothermality for the three components. The results are also shown in Table 3. The luminosity of the “cluster” component is  $4.5 \times 10^{44}$  erg/s and

dominates the total luminosity. We consider that the emission of G2 can be attributed to an elliptical galaxy because our derived luminosity is within the scatter of other ellipticals (Fabbiano et al. 1992; Matsushita 2001) and there is a good positional coincidence with the member elliptical galaxy, #362. On the other hand the luminosity of the G1 component is higher for a typical elliptical galaxy and the core radius is also comparable to that of other cluster with a small core radius (Ota & Mitsuda 2002). We will discuss the properties of the G1 component in more detail later.

Furthermore, we tested the significance of the ellipticity of the cluster image by substituting the third component in equation 1 for the elliptical  $\beta$ -model. We found the ellipticity is not significant; the 90% upper limit was  $\epsilon < 0.2$ . On the other hand, Soucail et al. (2000) and Böhringer et al. (2000) reported that the HRI image is slightly elongated in a northeast-southwest direction and can be fitted with a ellipse with an ellipticity of  $\sim 0.2 - 0.3$ . Soucail et al. (2000) also mentioned that there is a significant twist of the position angle at about 100 kpc from the center. We consider that the significant shift of the center position of cluster emission by 80 kpc and the presence of the second peak at 100 kpc off of the strongest peak in the *Chandra* image can account for the moderate ellipticity and the twist derived by the elliptical model analysis with the HRI.

## 5. MASS ESTIMATION AND COMPARISON

In this section we will derive the projected cluster mass profiles based on the results of the X-ray analysis and estimate the cluster mass enclosed within the arc radius. We will directly compare these with the results from the lensing mass reconstruction.

### 5.1. X-ray mass for the $\beta$ -model

From the spectral and spatial analysis with *Chandra*, we found that the cluster gas is consistent with being isothermal and can be described with the spherical  $\beta$ -model after removing the local emission of G1 and G2. In what follows, we regard the “cluster” component,  $i = 3$  in the three  $\beta$ -model fit, as diffuse emission coming from the ICM confined in the cluster dark matter potential. Since the G1 core radius is much smaller than the arc radius ( $r_{c,1} \ll r_{\text{arc}}$ ), while the cluster core radius  $r_{c,3} \sim r_{\text{arc}}$ , the G1 component is thought to be a minor contributor to the X-ray mass estimation. The effect of including the G1 mass will be discussed later in this section.

Assuming the gas is isothermal and spherically distributed and in hydrostatic equilibrium, the density of matter at a radius  $r$  is estimated from the  $\beta$ -model as

$$\rho_\beta(r) = \frac{3kT\beta}{4\pi r^2 G\bar{m}} \left[ \frac{3r^2}{r^2 + r_c^2} - \frac{2r^4}{(r^2 + r_c^2)^2} \right]. \quad (2)$$

The projected X-ray mass density profile is given by

$$\Sigma_{X,\beta}(R) = \int_{-\infty}^{\infty} \rho_\beta(\sqrt{R^2 + z^2}) dz = \frac{3kT\beta}{4G\bar{m}} \left[ \frac{R^2 + 2r_c^2}{(R^2 + r_c^2)^{3/2}} \right]. \quad (3)$$

In Figure 7 we show the mass density profile calculated for  $\beta$ -model. The cylindrical cluster mass within a certain radius  $R$  is calculated by integrating the projected density

profile, which can be written as follows (Ota et al. 1998).

$$M_{X,\beta}(R) = \frac{3kT\beta\pi}{G\bar{m}} \frac{R^2}{2\sqrt{R^2 + r_c^2}} \quad (4)$$

Then from the results of 2D fitting for the cluster component we estimated the X-ray mass within the arc radius of  $R_{\text{arc}} = 35'' = 220 h_{50}^{-1}$  kpc to be

$$M_{X,\beta}(220 h_{50}^{-1}\text{kpc}) = 0.84^{+0.20}_{-0.13} \times 10^{14} h_{50}^{-1} M_\odot. \quad (5)$$

Because the statistical errors of  $\beta$  and  $r_c$  are coupled with one another (Figure 6) though  $kT$  is independently determined from the  $\beta$ -model parameters, we determined the error associated with the X-ray mass by evaluating it in the statistically allowed domain of the three dimensional parameter space.

On the other hand, adopting the arc redshift of  $z_{\text{arc}} = 1.675$ , the strong lensing mass is estimated to be

$$M_{\text{lens}}(< 214 h_{50}^{-1}\text{kpc}) = (3.117 \pm 0.004) \times 10^{14} h_{50}^{-1} M_\odot \quad (6)$$

from equation (2) in Tyson et al. (1998). Broadhurst et al. (2000) derived the strong lensing mass as  $M_{\text{lens}}(< 200 h_{50}^{-1}\text{kpc}) = (2.22 \pm 0.06) \times 10^{14} h_{50}^{-1} M_\odot$ , which is smaller by about 30% than equation 6. However, comparing  $M_{X,\beta}$  to  $M_{\text{lens}}$ , a mass discrepancy of a factor of 3 is evident.

As shown in Figure 7, since the surface mass density of the cluster component obtained by the isothermal  $\beta$ -model is less than the critical surface mass density,  $\Sigma_{\text{crit}} = (c^2/4\pi G)/(D_s/D_d D_{ds}) = 2.1 \times 10^3 M_\odot/\text{pc}^2$  everywhere, the existence of the gravitationally multiple images in this cluster means that the mass distribution of the cluster is far from the isothermal  $\beta$ -model and/or the existence of an extra mass component along the line of sight toward the cluster central region is required.

### 5.2. X-ray mass for the NFW-model

The X-ray surface brightness profile of the NFW potential (Navarro et al. 1996) is similar to that of the  $\beta$ -model and can be converted from the  $\beta$ -model parameters through the relations of  $r_s = r_c/0.22$  and  $B = 15\beta$  (Makino et al. 1998). We thus derived the NFW density profile based on the results of  $\beta$ -model fitting,

$$\rho_{\text{NFW}}(r) = \frac{\rho_s r_s}{r(1 + \frac{r}{r_s})^2}, \quad (7)$$

where  $\rho_s = kTB/4\pi G\bar{m}r_s^2$ . We then calculated the projected mass density profile in the same manner as equation 3. The mass density profile is much steeper at the innermost region than that of the  $\beta$ -model and the central surface mass density can be higher than the critical surface mass density, however, those two models are not distinguishable at the arc radius (Figure 7). We estimated the X-ray mass to be

$$M_{X,\text{NFW}}(220 h_{50}^{-1}\text{kpc}) = 0.74^{+0.18}_{-0.11} \times 10^{14} h_{50}^{-1} M_\odot. \quad (8)$$

This shows that the NFW model does not improve the enclosed mass within the arc radius. Therefore, adopting the NFW model can not be the main solution for the mass discrepancy problem of this cluster.

### 5.3. Estimation of mass associated with G1

We will estimate the projected mass associated with the G1 component under some simple assumptions for the purpose of constraining its possible contribution to the X-ray mass estimate. Firstly, we consider the mass of the two bright elliptical galaxies inside G1. Their velocity dispersions and effective radii were measured to be  $\sigma = 317$  km/s and  $r_e = 5.9 h_{50}^{-1}$  kpc for #380 and  $\sigma = 275$  km/s, and  $r_e = 3.4 h_{50}^{-1}$  kpc for #374, respectively (van Dokkum et al. 1996). Then calculating the projected lensing mass under the Singular Isothermal Sphere model, we obtain  $M_{\text{SIS}} \sim \pi \sigma^2 / (2G r_e) = 4.4 \times 10^{11} M_\odot$  for #380 and  $M_{\text{SIS}} = 1.9 \times 10^{11} M_\odot$  for #374. Thus the sum of the two galaxies can increase  $M_X$  by only 1%.

Second, we will treat the G1 component as the cluster scale substructure embedded in or projected on the cluster. One reason in support of the idea is that the observed X-ray properties such as the temperature, the luminosity and the core radius all exceed those observed for a typical elliptical galaxy and they are rather close to a single cluster. However there is no unique way to evaluate this component in the  $M_X$  estimation, as it is not clear how this is physically related to the surrounding ICM. Thus our estimate of the G1 mass supposes that it is locally in hydrostatic equilibrium and dominates the mass out to a certain cutoff radius ( $r_{\text{cut}} \sim 100 h_{50}^{-1}$  kpc) at which the inflection in the X-ray surface brightness is found. Thereby we obtain  $M_{\text{G1}}(100 h_{50}^{-1}$  kpc) =  $0.51^{+0.20}_{-0.14} \times 10^{14} h_{50}^{-1} M_\odot$  utilizing equation 4 and the measured temperature within a radius of 8'' circle centered on G1. Adding  $M_{\text{G1}}$  to equation 5, we obtain  $M_{X,\beta} \lesssim 1.7 \times 10^{14} h_{50}^{-1} M_\odot$ . We consider this will give a secure upper limit of the X-ray mass estimation under the current isothermal  $\beta$ -model analysis. The total gas mass associated with the G1 clump within a sphere of  $r = r_{\text{cut}}$  is  $M_{\text{gas,G1}}(100 h_{50}^{-1}$  kpc) =  $5.7^{+1.8}_{-1.5} \times 10^{11} h_{50}^{-5/2} M_\odot$  and has a negligible contribution to the total gravitating mass. Thus this upper limit is still significantly smaller than  $M_{\text{lens}}$  by a factor of  $\sim 2$ . If we compare to the Broadhurst et al.'s mass, the discrepancy reduces to about 30%.

We drew critical lines of the lens model for a source at  $z = 1.675$  where the cluster component and the G1 component are included (Figure 8). The surface mass distribution of the G1 component is described by the equations (2) and (3) with above parameters for  $r < r_{\text{cut}}$  where  $r$  is the projected radius from the G1 center. The surface mass density beyond  $r_{\text{cut}}$  is assumed to be zero. Other parameters are the same as in §5.1. Inclusion of the G1 component turns the isothermal  $\beta$ -model into the super-critical and a tangential critical line appears. Thus G1 has a significant contribution to the lensing effect. Moreover we notice that  $r_{c,1}$  is fairly close to the core size of the dark matter distribution found in Tyson et al. (1998). We then consider that this also assures the significance of the existence of the G1 potential. If the lens model is able to explain the observed multiple images, the image appearing on the same side of the central image, which is in the south-east side from the cluster center (i.e. image B in Figure 8), should be enclosed by the tangential critical line. However, the inclusion of the G1 component described above is not enough to explain the observed lensed multiple images because the tangential critical line can not reach the south-east image.

### 5.4. Cluster center position

Next we directly compare the cluster center position derived by the X-ray image analysis to that of dark matter profile modeled by Tyson et al. (1998). We found that their center coordinates, (00:23:56.6, +16:53:15) (1950) are shifted if comparing their Figure 2 to the latest optical coordinates of central bright ellipticals from Czoske et al. (2001). Thus utilizing the coordinates of galaxy #380 in Czoske et al. (2001) and the relative distance from #380 galaxy to the DM center, 1''.5 to the east and 4''.5 to the south, the DM center coordinates correspond to about (00:26:35.8, +17:09:39.4) in J2000. Thus we found that the X-ray center position (00:26:35.6, +17:09:35.2) is shifted to the south-southwest by 4'' from the dark matter center. If we take into account the measurement uncertainties of  $\sim 2''$ , we consider that the shift is marginal. Moreover Tyson et al. (1998) derived the maximum point of diffuse intracluster light that is not associated with visible galaxies and showed it is displaced 3'' west-southwest from the DM center. The X-ray center position is closer to this than the DM center.

## 6. DISCUSSION

### 6.1. Properties of the intracluster gas

We will discuss the X-ray properties of the gas focusing on the X-ray luminosity-temperature ( $L_X - T$ ) relation, gas-mass fraction and the metallicity based on the *Chandra* analysis.

The location of the cluster on the  $L_X - T$  plane will provide important information for understanding the physical status of the ICM in the cluster central region. The observational data of clusters are known to exhibit a large scatter around the best-fit power-law model. Fabian et al. (1994) noted that the  $L_X - T$  relation is roughly divided into two sequences whether the clusters are XD or non-XD. The XD cluster is the cluster in which the X-ray emission is highly concentrated in the central giant elliptical galaxy and the X-ray peak position coincides with the center of the central galaxy. In the non-XD cluster, the emission is diffuse and the X-ray peak position is largely offset from the central giant galaxy. Arnaud & Evrard (1999) derived the  $L_X - T$  relation with the analysis sample restricted to non-XD clusters and showed a smaller scatter. A different approach was taken by Ota & Mitsuda (2002), concerning the cluster core radius. They performed a systematic analysis of 79 distant clusters with the *ROSAT* HRI and *ASCA* to study the X-ray structure of clusters in  $0.1 < z < 1$ . They determined the average X-ray temperatures and the bolometric luminosities with *ASCA* and the X-ray surface brightness distributions with the *ROSAT* HRI by utilizing the isothermal  $\beta$ -model, and found there is not any significant redshift dependence in the X-ray parameters including the temperature,  $\beta$ -model parameters, and the central electron density. They discovered that the distribution of the core radius shows distinct two peaks at 60 kpc and 220 kpc. If dividing the cluster samples into two subgroups corresponding to the two peaks in the core radius distribution, they show differences in the X-ray and optical morphologies and in the  $L_X - T$  relation. In particular, the normalization factor of the  $L_X - T$  relation

significantly differs according to the core sizes: at a certain temperature, the luminosity is higher for a cluster with small core radius and approximately  $L_X$  follows  $r_c^{-1}$ . From these observational results, they suggested that the clusters are divided into at least two subgroups according to the core radius. In §4, we showed that the X-ray spatial distribution of CL0024+17 is described with a superposition of two  $\beta$ -model components with  $r_{c,1} \sim 50$  kpc and  $r_{c,3} \sim 210$  kpc. Therefore, the main cluster component is classified as a non-XD cluster or a large core radius cluster, while the G1 component is classified as an XD or a small core radius cluster.

We will compare our result for CL0024+17 with Arnaud & Evrard (1999) and Ota & Mitsuda (2002). First, employing the  $L_X - T$  relation of Arnaud & Evrard (1999), the luminosity is expected to be  $\log L_X = 44.69 \pm 0.05$  for the observed temperature of 4.5 keV. Thus the X-ray luminosity of CL0024+17 determined with *Chandra*,  $\log L_{X,\text{bol}} = 44.7$ , is in a good agreement. Moreover, we compare our result to the  $L_X - T$  relation for clusters with large ( $r_c > 135$  kpc) core, derived by Ota & Mitsuda (2002) since the main cluster component whose core is  $r_{c,3} \sim 210$  kpc is responsible for the cluster luminosity (See Table 3). We found that the luminosity of CL0024+17 is smaller than the other distant cluster samples with similar temperatures, however, it is within a scatter of the data points and is quite consistent with the mean relation of the large core ( $r_c > 135$  kpc) clusters. Therefore in terms of the  $L_X - T$  relation, the X-ray emission of CL0024+17 agrees with other clusters that do not have strong central X-ray emission dominating the total luminosity. Adopting the estimated G1 luminosity of  $5.5 \times 10^{43}$  erg/s (Table 3), the temperature of 1.2 keV is obtained from the  $L_X - T$  relation for the small core radius clusters. The obtained temperature is significantly lower than that constrained by the X-ray observation (§3.2). This might be the signature that the G1 component is now in the process of merging with a cluster or has undergone a recent merger and therefore the characteristics of the G1 component can not be estimated by using a relation for relaxed clusters.

Since the observed X-ray spectrum is well fitted with the single-temperature MEKAL model (§3), the contribution of additional cool emission is suggested to be not important in this cluster. We can then estimate the time scale of radiative cooling at the cluster center. By deprojecting the central surface brightness of the  $\beta$  profile, we obtained the central electron density for the cluster component as  $n_{e0,3} = (5.8 \pm 0.6) \times 10^{-3}$  cm $^{-3}$ . Then the cooling time scale is 11.4 Gyr at the center. This is longer than the age of the Universe, 7.9 Gyr. Thus radiative cooling is not likely to be effective. On the other hand, the electron density is higher for G1, where  $n_{e0,1} = (2.5 \pm 0.5) \times 10^{-2}$  cm $^{-3}$ . This yields a much shorter cooling time of 2.8 Gyr. Thus cooling may occur very effectively in the G1 region. However it is contradictory that we did not find a significant temperature decrement in the spectral analysis (See §3.2). A similar situation has been found in some nearby clusters with short cooling timescales (e.g. Tamura et al. 2001) and other possibilities to prevent cooling have been proposed (e.g. Böhringer et al. 2002). We will discuss the possibility of a two-phase state of the ICM in the next subsection in detail.

We estimate the gas-mass fraction in the cluster within the virial radius in order to compare it with the mean baryon fraction in the Universe determined by the Wilkinson Microwave Anisotropy Probe (WMAP) experiments (Spergel et al. 2003). In this analysis, we use the standard set of the cosmological parameters determined by WMAP,  $\Omega_m = 0.3$ ,  $\Omega_\Lambda = 0.7$ , and  $h = 0.7$ . The virial radius is defined as the radius at which the cluster density is equal to 200 times the critical density of the universe at the cluster redshift,  $r_{200} = 1.39 h_{0.7}^{-1}$  Mpc. Then the virial mass (the spherical hydrostatic mass), gas mass and gas-mass fraction calculated at  $r_{200}$  under the  $\beta$ -model are

$$M_{200} = 4.6_{-0.9}^{+1.4} \times 10^{14} h_{0.7}^{-1} M_\odot, \quad (9)$$

$$M_{\text{gas}} = 6.5_{-0.6}^{+0.6} \times 10^{13} h_{0.7}^{-5/2} M_\odot, \quad (10)$$

$$f_{\text{gas}} = M_{\text{gas}}/M_{200} = 0.14_{-0.04}^{+0.05} h_{0.7}^{-3/2}. \quad (11)$$

The gas-mass fraction at the virial radius is consistent with the Universal baryon fraction derived by WMAP,  $\Omega_b/\Omega_m = 0.16$ , within 35% accuracy. Thus we consider the virial mass to be properly evaluated with  $M_{200}$  and the X-ray temperature to represent the virial temperature of the cluster potential.

As shown in the spectral analysis, the average iron abundance is about twice as high as the typical value. Since the metallicity is a quantity defined relatively to the amount of hydrogen, there are two situations that will explain this high value: a medium rich in iron or a medium poor in hydrogen. Because the gas-mass fraction (Equation 11) is comparable to that observed in other clusters (Mohr et al. 1999; Ota & Mitsuda 2001), it is plausible that the ICM was highly enriched in iron. As for nearby clusters, the iron mass in ICM,  $M_{\text{Fe}}$ , is known to have a clear correlation with the optical luminosity of E+S0 members (Arnaud et al. 1992) and with the total blue luminosity (Renzini 1997). Schneider et al. (1986) mentioned that the luminosity of CL0024+17 places it among the richest of any known clusters. Because the previous measurement of the cluster metallicity showed no significant redshift evolution (e.g. Mushotzky & Loewenstein 1997), and as the contribution of the metal production by type Ia SNe after  $z = 0.4$  can be negligible according to the model calculation by Mihara & Takahara (1994), we will compare the iron mass observed at  $z = 0.395$  to the optical luminosity corrected for passive evolution in ellipticals below. Utilizing the local relation,  $M_{\text{Fe}} \sim 1.6_{-1.1}^{+3.5} \times 10^{-2} L_{V,\text{E+S0}}^{1.0 \pm 0.30}$  (Arnaud et al. 1992) and the visual luminosity of ellipticals evolved to the present day  $L_V^{\text{E}}(z=0) = 1.2 \times 10^{12} h_{50}^{-2} L_\odot$  at  $r = 400 h_{50}^{-1}$  kpc (Smail et al. 1997), the iron mass is calculated as  $1.9_{-1.3}^{+4.2} \times 10^{10} h_{50}^{-2.5} M_\odot$ , where we adopted the best-fit slope of the  $M - L_{V,\text{E+S0}}$  relation, i.e. 1, and included only the  $1\sigma$  error of the normalization factor. Though the relation of Arnaud et al. (1992) was derived at a radius of  $3 h_{50}^{-1}$  Mpc, we assumed here that iron distribution is proportional to that of the galaxy and then it is applicable for a smaller radius. On the other hand, the *Chandra* analysis yields  $M_{\text{Fe}}(< 400 h_{50}^{-1}$  kpc) =  $(2.5 \pm 0.2) \times 10^{10} h_{50}^{-2.5} M_\odot$  where we adopted the mean metallicity measured within  $600 h_{50}^{-1}$  kpc, 0.76 solar. Because this is by about 30% higher than the above calculation, there may be an abundance variation from cluster to cluster, as suggested from the recent *Chandra* results of metallicity maps: the inho-

mogeneous metal distributions were found in the core regions of some nearby clusters such as Perseus (Schmidt, Fabian, & Sanders 2002) and A2199 (Johnstone et al. 2002). However, since the iron mass of CL0024+17 is consistent with the  $M_{\text{Fe}} - L_{V,\text{E+SO}}$  relation within the  $1\sigma$  errors, the variation is not statistically significant. To confirm this, we need future observations of the metallicity map with higher sensitivities.

The observed high metallicity can be explained by metal ejection from the elliptical galaxies. Since the spiral galaxy fraction,  $f_{\text{sp}} = 0.40$ , is not different from other clusters with a similar mass (Smail et al. 1997), the above result indicates that very effective galaxy formation had occurred in the central region of CL0024+17. Besides, the optical observations showed that the spatial distribution of galaxies is centrally concentrated and has a very compact core (Smail et al. 1996; Schneider et al. 1986). Then because of the high concentration of bright elliptical galaxies the metal will also follow the concentrated distribution. As mentioned above, there may also be a complex metal distribution in the cluster core. However due to the poor photon statistics, we are not able to derive the 2-dimensional abundance map. For this reason we studied the radially-averaged abundance profile in §3.2. Our result shown in Figure 3b indicates that the metal abundance is as high as  $\sim 1$  solar at the innermost region and then not in conflict with an abundance profile in which  $Z_{\text{Fe}} \sim 1$  within the central  $r \lesssim 10''$  region and  $Z_{\text{Fe}} \sim 0.3$  at the outer region. In order to further constrain the spatial distribution and the history of the metal production, better photon statistics for the X-ray spectrum are required.

## 6.2. Mass discrepancy problem

We found from the *Chandra* observation that the X-ray surface brightness distribution is mainly described by a superposition of two extended components well fitted with spherical  $\beta$ -profiles. Furthermore we do not find any significant temperature structure. Thus it is likely that the gas is relaxed in the cluster potential and, therefore, that hydrostatic equilibrium will be a good approximation in the X-ray mass estimation. We further discuss any possible cause of the mass discrepancy below.

As shown in the previous section, we can consider that the X-ray temperature represents the virial temperature of the cluster component since the gas mass fraction of the cluster component within the virial radius is consistent with the universal baryon fraction obtained by WMAP. Therefore, the mass discrepancy reported in the previous section is telling us that there is a lack of our current understanding for the nature of the cluster central region.

In some nearby clusters, particularly XD clusters (Forman & Jones 1990), an additional cool component is required to explain the X-ray emission of the central  $\sim 100 h_{50}^{-1}$ kpc regions (Makishima et al. 2001). On the contrary Makishima et al. (2001) also suggested that non-XD clusters appear to be isothermal with little metallicity gradient toward the center. Taking into account the fact that the current target cluster is a non-XD cluster and that the total X-ray emission is not dominated by the central G1 emission, our results shown in §3 seem to be more consistent with their picture of non-XD systems. However if the ICM of CL0024+17 is in a two-phase state and the thermal

pressure of the gas in each phase balances against gravitation, it would greatly increase the X-ray mass estimation. Thus we attempted to fit the spectra for both (1) the cluster region outside 100 kpc from G1, i.e.  $0''.26 < r < 1''.5$  and (2) the G1 region,  $r < 0''.26$  with a two-component MEKAL model. Because we are not able to constrain the two temperatures simultaneously under the current photon statistics, we fixed the temperature and the metallicity for the cool phase respectively at 1 keV and 1 solar while the spectral normalization was adjustable. For the region (1), we found that the flux of the cool phase is only about 4% of the hot phase and the temperature of the hot-phase is 5.5 (4.4 – 7.2) keV, which is consistent with the result of the single-phase model shown in Table 1 within errors. Thus the spectrum is well represented by the single-phase model. This is also consistent with the results of nearby non-XD clusters. For the region (2), because the radiative cooling time scale of the G1 emission is shorter than the age of the Universe (See §6.1), the gas might be in a two-phase state. However, from the two-phase model fitting, we found that the upper limit of the cool-phase flux is less than 1% of the hot-phase and the hot-phase temperature, 4.2 (3.5 – 5.3) keV, is again consistent with that obtained for the single-phase model. Thus we consider that it is unlikely that the G1 gas is in a two-phase state and that the virial temperature is much higher than that derived from the single-phase model.

Czoske et al. (2001, 2002) measured the redshift distribution of galaxies in the direction of CL0024+17 and revealed the presence of foreground and background groups of galaxies that align along the line of sight. Czoske et al. (2002) suggested from their results that there was a high speed ( $\sim 3000$  km/s) collision between the CL0024+17 cluster and a second cluster with a mass about half that of the main cluster  $\sim 3$  Gyr ago. They suggested that taking into account the projection effect of the second cluster mass may solve the mass discrepancy problem. They also mentioned that during the collision the X-ray gas would be highly disturbed due to propagation of shock waves (e.g. Takizawa 1999) and hydrostatic equilibrium of the gas component will break down, however, after several Gyrs the gas will settle down to an equilibrium state. Roettiger et al. (1996) noted that, based on numerical simulations, the temperature structure is one of the strongest indicator of recent merger activity, however, we do not find any substantial temperature structure in the observational data as shown in Figure 3(a). We also found from the spectral analysis of the G1 peak that the temperature is still higher than 2.6 keV at the central  $r < 4''$  region. Thus our results show that the cluster is in the state of several Gyr after the merging, and the gas should have settled down to an equilibrium state and then trace the underlying dark matter potential, which is supportive of Czoske et al. (2002)'s scenario.

As discussed above, the total cluster mass is considered to be properly evaluated from the X-ray observations at the virial radius based on the consistency of the gas-mass fraction with the Universal baryon fraction. On the other hand, the large mass discrepancy detected in the central region may indicate that there was a merging along the line of sight which disturbs the mass distribution in the cluster core region, as suggested by Czoske et al. (2002).

The G1 peak that we found in the X-ray image may be related with the merging. In addition if we are seeing the two collided cores superposed along the line of sight, the mean redshift values may be slightly different between the cores. However we could not constrain the redshifts of the G1 and the surrounding region from the X-ray spectral data under the current limited photon statistics and the energy resolution for the Fe line emission. We expect that the future *ASTRO-E2* mission will constrain the line-of-sight structure of the cluster mass distribution with its finest spectral resolution.

Although the previous precise lens modelings (Tyson et al. 1998; Broadhurst et al. 2000) were performed with an a priori assumption that CL0024+17 is an isolated single cluster of galaxies, our results have provided new evidences which show that this is not the case. One of the strongest pieces of evidence is the consistency of the gas-mass fraction of this cluster obtained from our X-ray results with the universal baryon fraction. In the case that the previous lens models (Tyson et al. 1998; Broadhurst et al. 2000) describe the cluster mass distribution up to the virial radius correctly, the gas mass fraction falls to 1/3 of the universal baryon fraction. Thereby it will be a key subject to construct a new lens model based on the current X-ray results and the results of the optical redshift survey by Czoske et al. (2002) which suggests the existence of the merger in the line of sight, and to examine the details of the physical nature of the G1 component by further X-ray observations.

## 7. SUMMARY

With *Chandra* we have performed the spectral and the spatial analysis of the lensing cluster CL0024+17. The temperature profile is consistent with being isothermal and the average temperature is  $\sim 4.5$  keV. We detected a strong redshifted iron line with a corresponding iron abundance of  $\sim 0.8$  solar, which is one of the largest values among known clusters. We found that the radial X-ray surface brightness distribution is not fitted with a single-component  $\beta$ -model or an NFW-SSM model and

that there is significant excess emission centered at central bright elliptical galaxy. The X-ray surface brightness distribution was well described by a 2-dimensional  $\beta$ -model of two extended components: the G1 component with a small ( $\sim 50$  kpc) core radius and the surrounding main cluster component with a core radius  $\sim 210$  kpc and whose center is shifted by  $\sim 80$  kpc from the G1 center. We derived the X-ray mass within the arc radius assuming hydrostatic equilibrium and compared it to the strong lensing mass. Our result clearly showed that the X-ray mass is significantly smaller by a factor of 2–3. We then discussed the possible cause of the mass discrepancy concerning the two-phase spectral model, the cluster merging and the effect of the secondary potential in the lensing effect. Although we do not rule out the possibility that G1 is a remnant of a cluster merger, because of the absence of any substantial temperature structure indicative of a recent merger the gas seems to have relaxed in the cluster potential. It is also true that G1 plays an indispensable role to make the surface mass density of the lens supercritical, however it is not sufficient to reconcile the large mass discrepancy. Considering the fact that the X-ray measurement of the gas-mass fraction at the virial radius is consistent with the universal baryon fraction, we suggest that it is important to further study the physical nature of the cluster core and clarify its relation to the merging process, and incorporate it into constructing a new lens model together with the latest optical information of the galaxy distribution.

We are grateful to S. Sasaki, T. Kitayama, and K. Masai for useful discussions and to K. Mihara and K. Shimasaku for suggestions related to the chemical evolution of galaxies. We thank G. Soucail for providing us the CFHT image of the cluster. We also thank P. G. Edwards for his careful review of the manuscript. N.O. is supported by a Research Fellowship for Young Scientists from the JSPS. N.O. acknowledges Hayashi Memorial Foundation for Female Natural Scientists. We thank the anonymous referee for constructive comments.

## REFERENCES

- Anders, E., & Grevesse, N. 1989, Geochim. Cosmochim. Acta, 53, 197
- Arnaud, M., Rothenflug, R., Boulade, O., Vigroux, L., & Vangioni-Flam, E. 1992, A&A, 254, 49
- Arnaud, M., & Evrard, A. E. 1999, MNRAS, 305, 631
- Böhringer, H., Soucail, G., Mellier, Y., Ikebe, Y., & Schuecker, P. 2000 A&A, 353, 124
- Böhringer, H., Matsushita, K., Churazov, E., Ikebe, Y., & Chen, Y. 2002, A&A, 328, 804
- Bonnet, H., Mellier, Y., & Fort, B. 1994, ApJ, 427, L83
- Broadhurst, T., Huang, X., Frye, B., & Ellis, R. 2000, ApJ, 534, L15
- Briel, U. G. et al. 1997, The ROSAT User's Handbook, (<http://www.xray.mpe.mpg.de/rosat/doc/ruh>)
- Butcher, H., & Oemler, A. Jr. 1978, ApJ, 219, 18
- Butcher, H., & Oemler, A. Jr. 1984, ApJ, 285, 426
- Cavaliere, A., & Fusco-Femiano, R. 1976, A&A, 49, 137
- Colley, W. N., Tyson, J. A., & Turner, E. L. 1996, ApJ, 461, L83
- Czoske, O., Kneib, J.-P., Soucail, G., Bridges, T.J., Mellier, Y., & Cuillandre, J.-C. 2001, A&A, 372, 391
- Czoske, O., Moore, B., Kneib, J.-P., & Soucail, G. 2002, A&A, 386, 31
- Dickey, J. M., & Lockman, F.J. 1990, ARA&A, 28, 215
- Dressler, A., & Gunn, J.E. 1992, ApJS, 78, 1
- Dressler, A., Smail, I., Poggianti, B. M., Butcher, H., Couch, W. J., Ellis, R. S., & Oemler, A. Jr. 1999, ApJS, 122, 51
- Fabbiano, G., Kim, D.-W., Trinchieri, G. 1992, ApJS, 80, 531
- Fabian, A.C., Crawford, C.S., Edge, A.C., Mushotzky, R.F. 1994, MNRAS, 267, 779
- Forman, W. & Jones, C. 1990, in STSI Symp. Series 4 Clusters of Galaxies, eds. W.R.Oegerle, M.J.Fitchett, L.Danly, 257.
- Green, P. J., Schartel, N., Anderson, S. F., Hewett, P. C., Foltz, C. B., Brinkmann, W., Fink, H., Trumper, J., Margon, B. 1995, ApJ, 450, 51
- Hashimoto-dani, K. 1999, Ph.D. Dissertation, Osaka University
- Hattori, M., Kneib, J.-P., Makino, N. 1999, Progress of Theoretical Physics Supplement, No. 133, p1
- Hewitt, J.N., Turner, E.L., Lawrence, C.R., Schneider, D.P., Gunn, J.E., Bennett, C.L., Burke, B.F., Mahoney, J.H., Langston, G.I., Schmidt, M., Oke, J.B., & Hoessel, J.G. 1987, ApJ, 321, 706
- Johnstone, R. M., Allen, S. W., Fabian, A. C., & Sanders, J. S. 2002, MNRAS, 336, 299
- Kaastra, J.S. 1992, An X-Ray Spectral Code for Optically Thin Plasmas (Internal SRON-Leiden Report, updated version 2.0)
- Kassiola, A., Kovner, I., & Fort, B. 1992, ApJ, 400, 41
- King, I.R. 1962, AJ, 67, 471
- Koo, D.C. 1988, in Large-Scale Motions in the Universe, V.G. Rubin and G.V. Cayne, Princeton University Press, p.513
- Liedahl, D.A., Osterheld, A.L., and Goldstein, W.H. 1995, ApJ, 438, L115
- Makino, N., Sasaki, S., & Suto, Y. 1998, ApJ, 497, 555

- Makishima, K., Ezawa, H., Fukazawa, Y., Honda, H., Ikebe, Y., Kamae, T., Kikuchi, K., Matsushita, K., Nakazawa, K., Ohashi, T., Takahashi, T., & Xu, H. 2001, PASJ, 53, 401
- Matsushita, K. 2001, ApJ, 547, 693
- Matsumoto, H., Tsuru, T.G., Fukazawa, Y., Hattori, M., & Davis, D.S. 2000, PASJ, 52, 153
- Mellier, Y., Fort, B., Soucail, G., Mathez, G., & Cailloux, M. 1991, ApJ, 380, 334
- Mewe, R., Gronenschild, E.H.B.M., and van den Oord, G.H.J. 1985, A&AS, 62, 197
- Mewe, R., Lemen, J.R., & van den Oord, G.H.J. 1986, A&AS, 65, 511
- Mihara, K., & Takahara, F. 1994, PASJ, 46, 447
- Miralda-Escudé, J., & Babul, A. 1995, ApJ, 449, 18
- Mushotzky, R.F., & Loewenstein, M. 1997, ApJ, 481, L63
- Mohr, J.J., Mathiesen, B., & Evrard, A.E. 1999, ApJ, 517, 627
- Moore, B., Gelato, S., Jenkins, A., Pearce, F. R., & Quilis, V. 2000, ApJ, 535, L21
- Navarro, J.F., Frenk, C.S., & White, S.D.M. 1996, ApJ, 462, 563
- Ota, N. 2001, Ph.D. thesis, University of Tokyo
- Ota, N., Mitsuda, K., & Fukazawa, Y. 1998, ApJ, 495, 170
- Ota, N., & Mitsuda, K. 2001, in ASP Conf. Ser. 251, New Century of X-ray Astronomy, ed. H. Inoue & H. Kunieda (San Francisco: ASP), 478
- Ota, N., & Mitsuda, K. 2002, ApJ, 567, L23
- Renzini, A. 1997, ApJ, 488, 35
- Roettgering, K., Burns, J. O., & Loken, C. 1996, ApJ, 473, 651
- Schmidt, R. W., Fabian, A. C., & Sanders, J. S. 2002, MNRAS, 337, 71
- Schneider, D. P., Dressler, A., & Gunn, J. E. 1986, AJ, 92, 523
- Shapiro, P. R., & Iliev, I. T. 2000, ApJ, 542, L1
- Smail, I., Dressler, A., Kneib, J.-P., Ellis, R.S., Couch W.J., Ray M.S., & Oemler, A. Jr., 1996, ApJ, 469, 508.
- Smail, I., Ellis, R.S., Dressler, A., Couch, W.J., Oemler, A. Jr., Ray, M.S., & Butcher, H. 1997, ApJ, 469, 508
- Spergel, D. N., & Steinhardt, P. J. 2000, Physical Review Letters, 84, 3760
- Spergel, D. N., Verde, L., Peiris, H. V., Komatsu, E., Nolta, M. R., Bennett, C. L., Halpern, M., Hinshaw, G., Jarosik, N., Kogut, A., Kimon, M., Meyer, S. S., Page, L., Tucker, G. S., Weiland, J. L., Wollack, E., & Wright, E. L., submitted to ApJ(astro-ph/0302209).
- Soucail, G., Ota, N., Böhringer, H., Czoske, O., Hattori, M., & Mellier, Y. 2000, A&A, 355, 433
- Suto, Y., Sasaki, S., & Makino, N. 1998, ApJ, 509, 544
- Takizawa, M. 1999, ApJ, 520, 514.
- Tamura, T., Kaastra, J.S., Peterson, J.R., Paerels, F.B.S., Mittaz, J.P.D., Trudolyubov, S.P., Stewart, G., Fabian, A.C., Mushotzky, R.F., Lumb, D.H., & Ikebe, Y 2001, A&A, 365, 87.
- Tyson, J.A., Kochanski, G.P., & Dell'Antonio, I.P. 1998, ApJ, 498, L107
- van Dokkum, P.G., & Franx, M. 1996 MNRAS, 281, 985
- Wu, X.-P., & Fang, L. Z. 1997, ApJ, 483, 62

FIG. 1.— X-ray image of CL0024+17 in the 0.5 – 7 keV band obtained with the *Chandra* ACIS-S3 with overlaid contours. The image is adaptively smoothed and corrected with the exposure map. The background is not subtracted. The image and the contours are logarithmically scaled. The point sources detected with the ROSAT HRI, S1–S5 (Soucail et al. 2000) are shown with the ROSAT error box of  $16'' \times 16''$ . The boundary of the ACIS-S3 CCD chip is shown with  $8' \times 8'$  box.

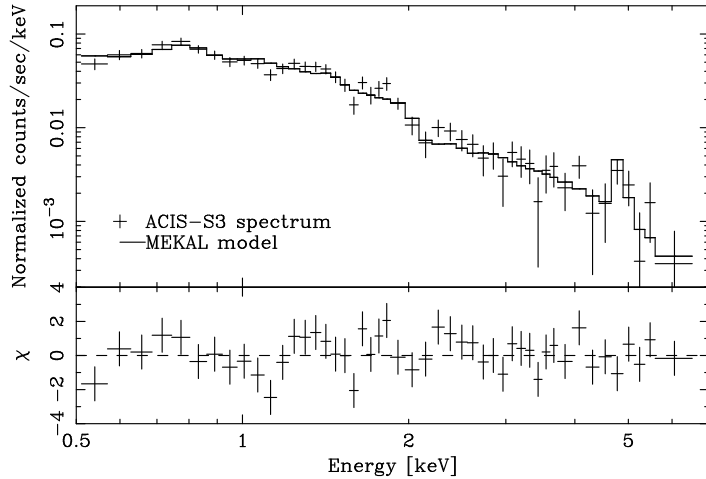


FIG. 2.— *Chandra* ACIS-S3 spectrum of CL0024+17 ( $r < 1'.5$ ) fitted with the MEKAL model. In the upper panel, the crosses denote the observed spectrum and the step function shows the best-fit model function convolved with the telescope and the detector response functions. In the lower panel, the residuals of the fit in units of  $\sigma$  are shown.

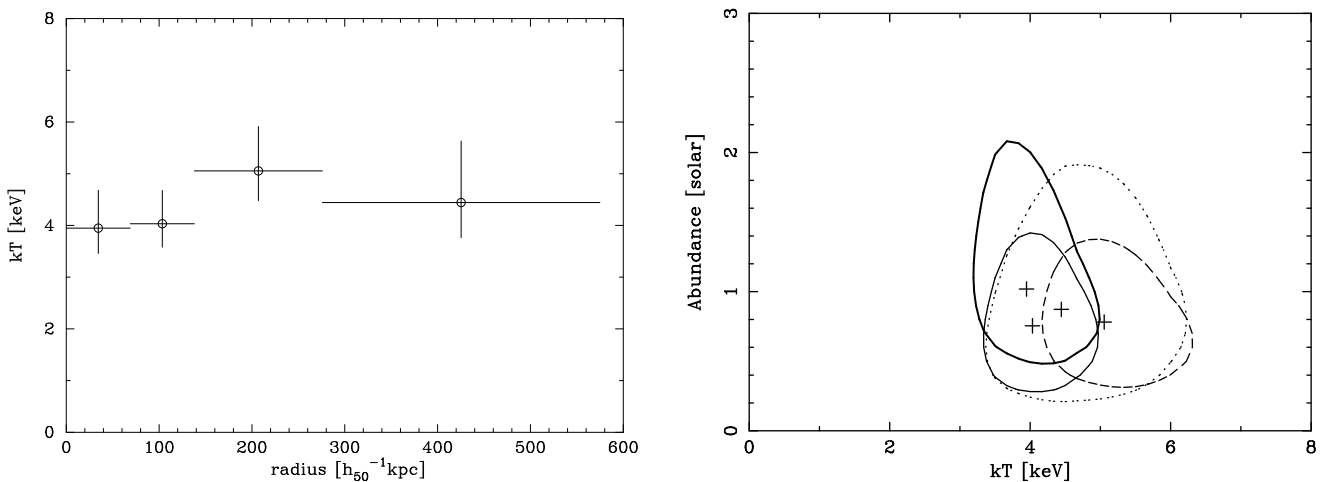


FIG. 3.— (a) Radial temperature profile determined from the MEKAL model fitting to the four annular regions. The vertical error bars are  $1\sigma$ . (b) Confidence contours of the temperature and the metal abundance for the same four annular regions used in the left panel. The single-parameter 68% error domains are shown as contours with the thick-solid, thin-solid, thin-dashed, thin-dotted lines from the inner to the outer annuli.

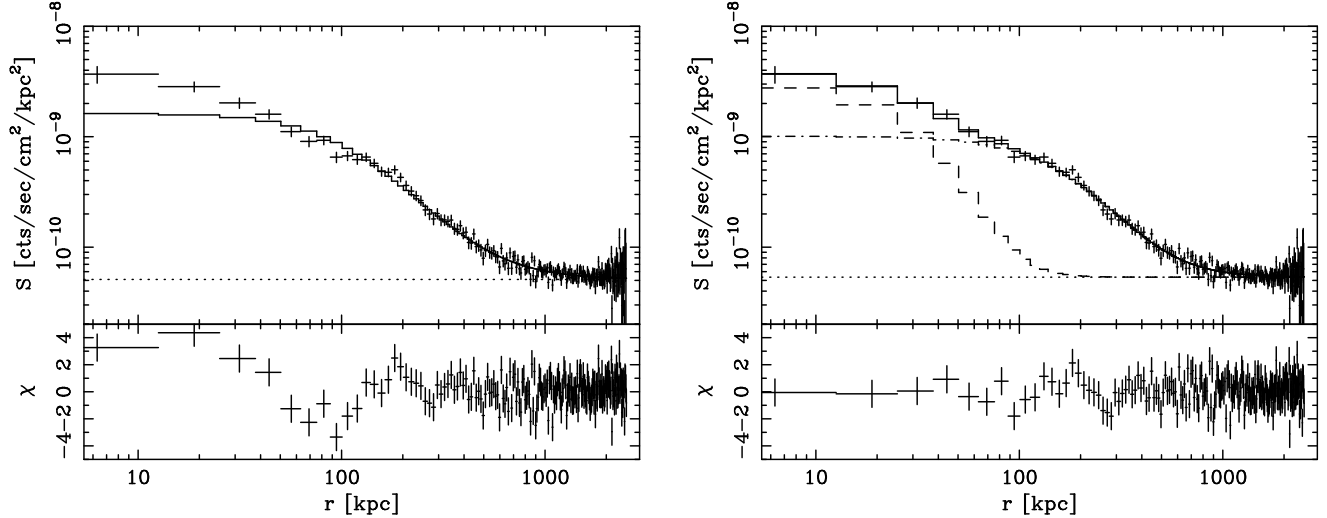


FIG. 4.— Results of the 1-dimensional surface brightness distribution fitting with the single  $\beta$  model (a) and the double  $\beta$  model (b). In each panel, the crosses show the observed surface brightness and the solid line shows the best-fit model. The constant background is shown with the horizontal dotted line. For the double  $\beta$  model, the inner and the outer components are respectively shown with the dashed and the dash-dotted lines.

FIG. 5.— Results of the 2-dimensional surface brightness distribution fitting with the three  $\beta$  profiles. (a) *Chandra* ACIS-S3 image of the central  $3'.3 \times 3'.3$  region of CL0024+17 in the  $0.5 - 5$  keV energy range. The small circles denote the positions of the galaxies with  $0.38 < z < 0.41$  (Czoske et al. 2001). A closer view of the central  $30'' \times 30''$  region is also shown in the upper-left panel. (b) The best-fit 2D image of the three  $\beta$ -models, overlaid by the contours with logarithmic spacing. (c) Residuals of the 2D image fitting. (d) Residuals projected to the  $x$ - and  $y$ -directions in units of  $\sigma$ .

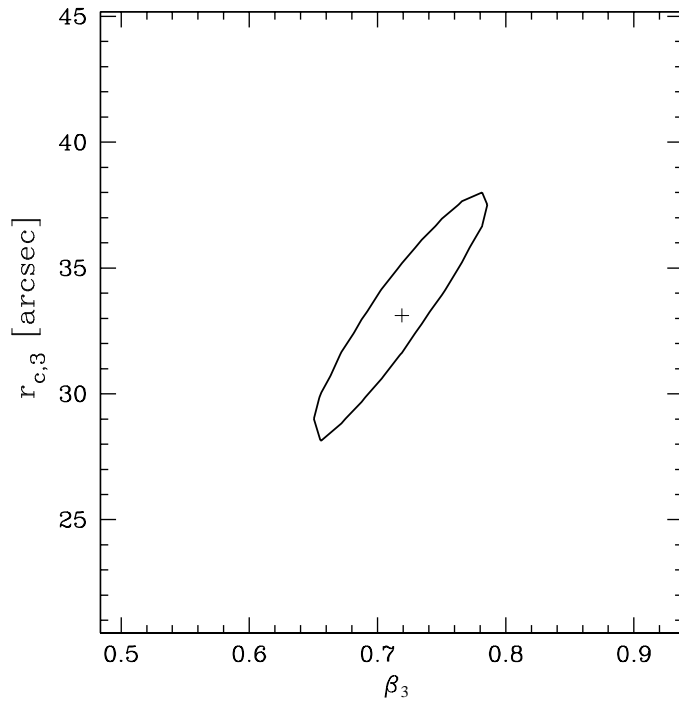


FIG. 6.—  $\chi^2$  contours of the 2-dimensional image fitting. The 90% single-parameter error domain for  $\beta_3$  and  $r_{c,3}$  of the cluster component is shown. The position of the  $\chi^2$  minimum is denoted with a cross.

FIG. 7.— X-ray mass density profiles for the  $\beta$ -model (the thick line) and the NFW model (the thin line) of the main cluster component. The 90% error ranges are shown with the dashed and the dotted lines, respectively. The arc radius of  $220h_{50}^{-1}\text{kpc}$  is denoted with the arrow. The projected dark matter density profile derived by Tyson et al. (1998) was plotted with the solid curve using the fitted parameters given by Shapiro & Iliev (2000). The critical surface density,  $\Sigma_{\text{crit}}$ , is indicated with the horizontal dash-dot line.

FIG. 8.— Critical lines for a source at  $z = 1.675$  are overlaid on the B band image of CL0024+17 obtained with CFHT (the original image was described in Czoske et al. (2001)). North is up and east is left. The multiple arc images are marked with A–E in the same manner as Colley et al. (1996). No critical line appears in the case of a cluster lens for the main cluster potential (see §5.1). On the other hand, when adding the G1 potential the critical lines appear (the inner and the outer curves are the radial and the tangential critical lines respectively), however, it is not enough to reach to the southeast image (see §5.3). The object numbers of the central elliptical galaxies in the catalog of Czoske et al. (2001) are also shown.

TABLE 1  
RESULTS OF THE MEKAL MODEL FITTING TO THE OVERALL SPECTRUM

Parameter	Value (90% error)
$N_{\text{H}}$ (cm $^{-2}$ )	$4.2 \times 10^{20}$ (F)
$kT$ (keV)	4.47 (3.93 – 5.30)
Abundance ( $Z_{\odot}$ )	0.76 (0.45 – 1.13)
Redshift	0.395 (F)
Normalization <sup>a</sup>	5.72 (5.20 – 6.25)
$\chi^2/\text{dof}$	47.5/45
$f_{\text{X},0.5-7}$ (erg/s/cm $^2$ ) <sup>b</sup>	$4.1 \times 10^{-13}$
$L_{\text{X},0.5-7}$ (erg/s) <sup>c</sup>	$3.4 \times 10^{44}$
$L_{\text{X,bol}}$ (erg/s) <sup>d</sup>	$5.1 \times 10^{44}$

<sup>a</sup>Normalization factor for the MEKAL model,  $\int n_e n_{\text{H}} dV / 4\pi D_A^2 (1+z)^2$  in  $10^{-18} \text{ cm}^{-5}$ , where  $D_A$  is angular size distance to the cluster.

<sup>b</sup>X-ray flux in the 0.5–7 keV band.

<sup>c</sup>X-ray luminosity in the 0.5–7 keV band.

<sup>d</sup>Bolometric luminosity.

(F) Fixed parameters.

TABLE 2  
RESULTS OF THE 1-D IMAGE FITTING

Model	(component)	$S_0^{\text{a}}$ cts/s/cm $^2$ /(h $^{-1}_{50}$ kpc) $^2$	$\beta$	$r_c$ "/h $^{-1}_{50}$ kpc	$\chi^2/\text{dof}$
Single- $\beta$		$1.6^{+0.3}_{-0.2} \times 10^{-9}$	$0.55^{+0.04}_{-0.04}$	$17.2^{+1.7}_{-1.6}/109^{+22}_{-20}$	242.5/196
Double- $\beta$	(inner)	$2.8^{+0.8}_{-0.7} \times 10^{-9}$	1.0(F)	$7.0^{+1.4}_{-1.4}/45^{+10}_{-9}$	183.2/194
	(outer)	$9.6^{+0.2}_{-0.1} \times 10^{-10}$	$0.66^{+0.08}_{-0.06}$	$29.5^{+6.0}_{-5.0}/187^{+38}_{-31}$	
Model	$\alpha$	$S_0^{\text{a}}$ cts/s/cm $^2$ /(h $^{-1}_{50}$ kpc) $^2$	$B$	$r_s$ "/h $^{-1}_{50}$ kpc	$\chi^2/\text{dof}$
NFW-SSM	1(F)	$1.8^{+0.3}_{-0.2} \times 10^{-9}$	$8.3^{+0.8}_{-0.6}$	$65^{+17}_{-13}/415^{+107}_{-86}$	229.3/196

(F) Fixed parameters.

<sup>a</sup>Central surface brightness of the  $\beta$ -profile or the NFW-SSM model in the 0.5 – 5 keV.

TABLE 3  
RESULTS OF THE 2-D IMAGE FITTING WITH THE THREE  $\beta$ -MODELS

Model	$i$	Center position RA,Dec in J2000	$S_{0,i}^{\text{a}}$ cts/s/cm $^2$ /(h $^{-1}_{50}$ kpc) $^2$	$\beta_i$	$r_{c,i}$ "/h $^{-1}_{50}$ kpc	$L_{\text{X,bol}}$ erg/s
G1	1	00:26:36.0,+17:09:45.9 (F)	$3.1^{+0.9}_{-0.6} \times 10^{-9}$	1 (F)	$8.3^{+1.7}_{-1.4}/52^{+11}_{-9}$	$5.5 \times 10^{43}$
G2	2	00:26:35.1,+17:09:38.0 (F)	$4.7^{+2.9}_{-2.5} \times 10^{-9}$	1 (F)	$1.6/10$ (F)	$3 \times 10^{42}$
Cluster	3	00:26:35.6,+17:09:35.2 <sup>b</sup>	$8.7^{+1.2}_{-0.9} \times 10^{-10}$	$0.71^{+0.07}_{-0.06}$	$32.8^{+5.1}_{-4.7}/210^{+33}_{-30}$	$4.5 \times 10^{44}$

(F) Fixed parameters.

<sup>a</sup>Central surface brightness of the  $\beta$ -profile in the 0.5 – 5 keV.

<sup>b</sup>The 90% errors are  $\pm 1''$ .3 for RA and  $\pm 1''$ .5 for Dec.

This figure "f1.jpg" is available in "jpg" format from:

<http://arXiv.org/ps/astro-ph/0306580v2>

This figure "f5.jpg" is available in "jpg" format from:

<http://arXiv.org/ps/astro-ph/0306580v2>

This figure "f7.jpg" is available in "jpg" format from:

<http://arXiv.org/ps/astro-ph/0306580v2>

This figure "f8.jpg" is available in "jpg" format from:

<http://arXiv.org/ps/astro-ph/0306580v2>